

Corrosion resistance of 625 nickel superalloy exposed to isothermal and thermal cycling conditions in a chloride/carbonate salt

Stuart Bell^{*}, Mitchell de Bruyn, Ted Steinberg, Geoffrey Will

School of Mechanical, Medical and Process Engineering, Science and Engineering Faculty, Queensland University of Technology, Brisbane 4001, QLD, Australia



ARTICLE INFO

Keywords:

Molten salt corrosion
Thermal energy storage
Nickel Superalloy
Thermal Cycling

ABSTRACT

Using phase change materials as thermal energy storage media is a promising approach for use in conjunction with concentrating solar thermal power (CSP) – particularly at the higher temperatures planned for next generation CSP. However, the corrosion resistance of high temperature alloys with the molten salt media proposed in these systems is critical for system longevity. The compatibility of alloy 625 in a eutectic salt mixture consisting of 59.5 wt% Na₂CO₃/40.5 wt% NaCl is investigated under isothermal conditions at 650 °C, and for thermal cycles between 600 and 650 °C.

Minimal thickness loss was detected as a protective oxide was produced on the metal surface. This dense, adherent oxide consisted of a nickel oxide outer oxide layer and a nickel-chromium inner oxide layer. No major dealloying was found with this salt/alloy combination, although relatively low concentrations of alloying elements were detected in the salt. Molybdenum, chromium and niobium were found in the salt at the highest concentrations relative to their availability in the alloy. Very little nickel was detected in the salt, corroborating the protective nature of the nickel oxide surface layer.

A corrosion rate of approximately 120–170 µm/year was determined for this alloy/salt combination, which was attributed to the oxide growth on the metal surface. As this oxide is protective, this corrosion rate will be significantly lower for long term exposure, potentially within the allowable corrosion rate for a thermal energy storage system.

1. Introduction

Thermal energy storage (TES) allows the power produced through concentrated solar power (CSP) systems to be dispatched when best suits the operators and the power grid. CSP systems in the future are proposed with receiver temperatures above 700 °C, and power block cycles input temperatures above 600 °C. Thus, for heat to flow from the receiver, through the TES and to the power block, TES needs to operate between 600 and 700 °C.

Molten salts with favourable thermophysical properties and low cost are an appealing choice for thermal energy storage. The inclusion of the latent heat of fusion in a phase change can increase storage energy density, reduce system size and therefore reduce cost. Phase change material (PCM) based TES systems differ from sensible heat storage (such as two tank or thermocline systems) in that the storage media remains stationary and a separate heat transfer fluid is used for charging

and discharging.

There are a number of eutectic salt mixtures with melting temperatures in the 600–700 °C range (Raud, 2018; Raud, 2018). One candidate, a mixture of Na₂CO₃/NaCl has properties which make it a good candidate for PCM based thermal energy storage and a very low cost in comparison to other thermal storage media, approximately 0.12 US\$/kg (Liu, 2021) compared to 0.5 US\$/kg for Solar Salt (Liu, 2016). Early studies identified that an eutectic mixture of 59.5 %wt Na₂CO₃/40.5 %wt NaCl has a melting point of 637 °C and a latent heat of around 283 J/g (Raud, 2018; Jiang, 2016). More recently a latent heat of 388 J/g has been identified with a 54.5 %wt Na₂CO₃/45.5 %wt NaCl ratio for this salt (Ong, 2021), yielding a latent heat/cost ratio above 3000 J/US\$.

The compatibility of containment materials with this salt under both isothermal and thermal cycling conditions is critical for designing TES systems for sufficient lifetime. The dissolution of the chromium into the salts has previously been identified as the major damage mechanism in

Abbreviations: TES, Thermal energy storage; CSP, concentrating solar power; PCM, phase change material; SEM, Scanning Electron Microscopy; EDS, Energy Dispersive X-ray Spectroscopy; ICP-MS, Inductively Coupled Plasma Mass Spectroscopy; ICP-OES, Inductively Coupled Plasma Optical Emission Spectroscopy.

* Corresponding author.

E-mail address: s2.bell@qut.edu.au (S. Bell).

<https://doi.org/10.1016/j.solener.2022.11.034>

Received 13 February 2022; Received in revised form 25 July 2022; Accepted 22 November 2022

Available online 5 December 2022

0038-092X/© 2022 International Solar Energy Society. Published by Elsevier Ltd. All rights reserved.

chloride and carbonate salts (Kruizenga, 2012; Frangini, 2008). Isothermally tested samples of 316 stainless steel fully immersed in the salt were found to be depleted of iron at grain boundaries while chromium is involved in the formation of a low adherence semi-protective oxide (Sarvghad et al., 2018). When samples were half immersed in the salt, depletion from grain boundaries at depths of 50–100 µm were found both above and below the salt (Sarvghad et al., 2017). When thermally cycled, 316L stainless steel produced thick corrosion scale with multiple layers (Liu, 2017). The outer iron oxide layer in contact with the salt was found to contain sodium, which indicates its ingress into the corrosion scale. Chromium content was found to increase in the oxide layers close to the metal, as chromium diffuses outward through the scale layers and is dissolved into the salt. ICP-OES analysis determined that both chromium and iron were present in the salt.

The structure and oxidation state of corrosion produced by this $\text{Na}_2\text{CO}_3/\text{NaCl}$ molten salt on 316L stainless steel, in both air and high purity argon environments was recently investigated (Bell, 2022). Using high purity argon as a cover gas resulted in significantly thinner scale and reduced the dissolution of alloying elements into the salt compared to air. Oxidation states were lower in the corrosion of the argon exposed samples, where only Cr^{2+} was identified. Whereas in air, both Cr^{2+} and Cr^{3+} were found in the inner chromium rich layer of the thick corrosion scale. This was attributed to the reduced basicity (O^{2-} ion activity) under argon, and the dissolution mechanism which removed the Cr^{3+} based ionic species (CrO_2^-) into the salt. Therefore, under certain circumstances, using a cover gas such as argon or nitrogen can change the salt chemistry and reduce corrosion.

TES systems which operate at temperatures above 600 °C also need to consider the strength of the containment material. Fig. 1 shows how the strength of steels is affected by temperature. The tensile strength of 316, which is 450 MPa at 600 °C, is reduced to less than a third – 190 MPa with a temperature increase to 800 °C. For stainless steels to be serviceable at temperatures above 600 °C, mechanical stress must be carefully considered in the storage design. If mechanical stress cannot be avoided, nickel superalloys will likely be required, with some authors suggesting that nickel superalloys are mandatory above 550 °C (Walczak, 2018). This is critical for phase change thermal energy storage systems, as the thermal cycle inherent in these systems will likely result in secondary (thermally induced) stresses in the system. Therefore, the compatibility of nickel superalloys with potential TES media, such as this molten salt is of interest to the solar thermal community.

This interest in nickel superalloys has resulted in various studies into

high strength nickel superalloys. A study into alloy 601 found chromium dealloying resulting in sample porosity at areas both submerged in the salt and exposed to air after a short 120 h test (Sarvghad et al., 2017). This chromium depletion was related to the presence of oxygen with 100 µm of porosity in oxygen exposed regions, and slightly less, around 80 µm in submerged regions.

Further testing of 601 alloy under isothermal and cycling conditions for exposure times up to 768 h found significant surface porosity from dealloying of chromium to depths of 150–180 µm (Bell, 2019). This was attributed to a non-protective, porous oxide which allowed molten salt to dissolve chromium directly from the metal under the oxide layer. When comparing the effect of isothermal testing with thermal cycling, the corrosion growth and the depletion rate were found to be proportional to the time that the salt was molten. Another alloy tested in the same study, Inconel C-276 was found to produce a thick, adherent oxide which protected the base alloy from the chloride/carbonate salt (Bell, 2022). Counter to the 601 study, chromium was not significantly dealloyed. Molybdenum, manganese and tungsten were the primary elements detected in the salt, but in significantly lower concentrations compared to chromium in the 601 study. The thickness of the oxide layers was reduced and chromium was only found in the salt when the temperature was cycled, probably due to spalling of the scale. However, no cracking or buckling was detected in the oxide layer which still protected the base alloy from direct attack by the salt.

Alloy 625 is a nickel based superalloy with very high strength above 600 °C (Fig. 1). It is a good candidate for testing of nickel superalloys containing significant molybdenum, niobium and low iron – an element which forms the problematic porous oxides identified in earlier studies (Bell, 2022; Bell, 2019).

While the superalloy 625 has not previously been tested in the chloride/carbonate eutectic salt used here, its resistance to corrosion in other molten salt mixtures has been investigated in several studies. Corrosion of alloy 625 was investigated in NaCl , KCl , MgCl_2 and CaCl_2 individually, and in various mixtures of those four salts, to determine the effect of the cation species (Ming, 2015). Unfortunately, hydrated MgCl_2 and CaCl_2 salts were used (these earth alkaline salts are notably hygroscopic) which ensured that any melts containing these materials were highly corrosive as they form HCl which chlorinates the structural metals, accelerating corrosion significantly (Sridharan et al., 2013; Bell et al., 2019). It is difficult to apply these results from this work to a TES system, and illustrates the importance of controlling impurity levels in salts in order to control corrosivity.

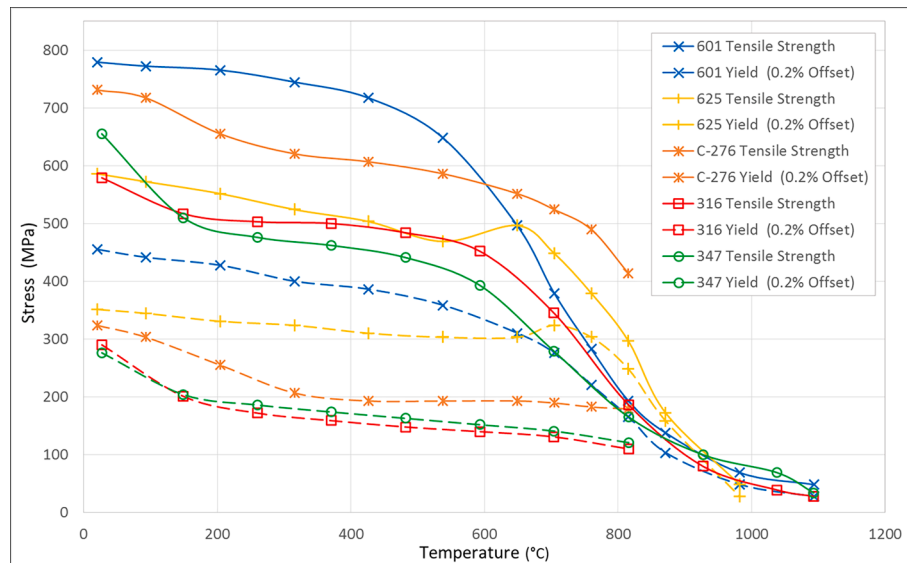


Fig. 1. Yield strength and Tensile Strength for 601, 625 and C-276 nickel superalloys (Special Metals) and 316 and 347 Stainless Steel alloys (American Iron and Steel Institute, 1979).

A work which demonstrates the potential for aggressive corrosion in chloride salts, even under controlled impurity conditions (Grégoire, 2020) found similar chromium dissolution mechanisms in Inconel 600 to those discussed earlier in the compositionally similar Inconel 601 (Bell, 2019). The 600 alloy was dealloyed to depths of up to 140 µm after 300 h exposure at 700 °C under argon with 5 ppm water and 2 ppm O₂. This attack was attributed to moisture based impurities reacting with MgCl₂ and forming corrosive MgOH⁺ ions, which selectively dissolve chromium and chromium rich carbides from the metal and into the salt.

Testing of 310 and 347 grade stainless steels, Incoloy 800H and Inconel 625 in a binary NaCl/LiCl salt found the 625 alloy to be the most corrosion resistant (Gomez-Vidal and Tirawat, 2016). A corrosion rate of 2.80 ± 0.38 mm/year was found for 625 under a nitrogen atmosphere using electrochemical methods – which tend to overestimate corrosion rates as they are short term and take place during the impurity driven corrosion regime. The greater corrosion resistance of 625 compared to the other alloys tested was attributed to its low iron and high nickel content.

A sister study to the above used electrochemical methods to investigate 310, 321, 347, Incoloy 800H, alumina-forming austenitic (AFA-OC6) and Inconel 625 in the molten carbonate eutectic salts K₂CO₃/Na₂CO₃ and Na₂CO₃/K₂CO₃/Li₂CO₃ (Gomez-Vidal et al., 2016). This study found that 800H, 310 and AFA-OC6 were the best performing alloys in the binary salt (750 °C under N₂) with Inconel 625 having a corrosion rate of 2.6 ± 0.59 mm/year. Higher temperatures significantly increased corrosion rates, whilst utilizing a CO₂ atmosphere to increase the stability of the salt slowed corrosion somewhat, but did not reduce corrosion rates to acceptable levels. Coating with thermally deposited MCrAlX coating however, showed some promise for isolating structural materials from this aggressive class of salt.

Nitrate salts, which are used in commercial TES, are limited to around 565 °C due to a decomposition reaction which results in reduced thermophysical properties and increased corrosion. Using nickel superalloys such as alloy 625 has attracted interest in an attempt to extend the useable temperature range of these salts. A recent study investigated corrosion on Inconel 625 in molten nitrate salts at 500 and 600 °C using gravimetric, electrochemical and microscopy methods (Khorsand, 2018). These tests were undertaken for very short test times – <2 days – and found that the corrosion obeyed a parabolic rate law. This was attributed to the corrosion being controlled by diffusion through the scale, which slows as the scale layer grows.

A long-term study into the corrosion of two low chromium steels, two stainless steels and Inconel 625 in solar salt at 600 °C found that 625 offered the best corrosion protection of the alloys tested (Soleimani Dorcheh et al., 2016). The 625 alloy produced a nickel–iron oxide layer approximately 15 µm thick after 5000 hrs exposure. Reaction kinetics found that the 625 lost mass linearly with time which was attributed to limited oxide spallation and dissolution into the molten salt.

McConohoy and Kruizenga investigated nitrate solar salt and corrosion of HA230 and Inconel 625 nickel superalloys at 600 °C and 680 °C. Both alloys were found to have good corrosion resistance at 600 °C, but at 680 °C the corrosion rates increased by a factor of about 30, with 625 performing slightly better than HA230 (16.8 to 594 µm/year for 625 and 23.6 to 688 µm/year for HA230). During the 600 °C test, the 625 formed a NiO layer approximately 10 µm thick, which is likely protective under these conditions. At 680 °C significant nitrite (NO₂) evolution was measured and an associated loss of latent heat and melting temperature in the salt was also observed.

Alloy 625 has also been tested in a FLiBe salt (a mixture of lithium and beryllium fluoride which is used in the nuclear sector) along with alloys 600 and C-276 (Kondo, 2009). Isothermal tests for 1000 h determined corrosion rates of 625 were the lowest of those tested – 1.1 µm/year and 1.0 µm/year at 500 and 600 °C respectively. The measured chromium level in the salt after testing was 120 wppm at 500 °C and 710 wppm at 600 °C, confirming dissolution of chromium was the major corrosion mechanism for this alloy/salt combination.

This paper investigates the corrosion resistance of 625 alloy in a NaCl/Na₂CO₃ eutectic salt to determine corrosion rate, structure and propensity of alloying elements to be dissolved by the salt. Both isothermal, and thermal cycling conditions were used with tests undertaken between 600 and 650 °C up to 768 h (32 days) under an air environment. These aggressive conditions were used to determine the alloy's resistance to corrosion and attack by the salt. Analysis of the corrosion rate was undertaken by thickness loss, measured from light microscopy. Corrosion structure was analysed using scanning electron microscopy and energy dispersive X-ray spectroscopy (SEM-EDS), whilst elemental analysis of the salt was determined using Inductively Coupled Plasma Mass spectroscopy (ICP-MS).

2. Method

The elemental composition of the alloy 625 metal was obtained from the supplier and is presented in Table 1. Immersion tests using the 55.3 %wt Na₂CO₃/44.7 %wt NaCl (analytical grade anhydrous salt - minimum assay; 99.7 % NaCl; 99.9 %Na₂CO₃ sourced from Chem-Supply) molten salt were undertaken under both isothermal conditions at 650 °C, and using a thermal cycle from 600 to 650 °C to produce a melt/freeze cycle. Pieces of wire approximately 3 cm in length and 2.4 mm in diameter were half submerged in 20.0 g of the salt in a 50 ml CN-0050 alumina crucible (obtained from Ceramic Oxide Fabricators). This replicated two conditions; metal in contact with bulk salt, and metal in contact with salt exposed to a high oxygen environment, due to the salt's propensity to "wet" metals and develop a thin coating of salt on the surface of the unsubmerged metal.

The isothermal and cycled test conditions used four samples each, which were removed at 96 h, 192 h, 384 h and 768 h. The experiments conducted are outlined in Table 2. These tests were undertaken using standard muffle furnaces obtained from Tetlow. The thermal cycling tests were undertaken in a furnace with controls modified so that a cycle between 600 °C and 650 °C every 2 h, with a 50 min hold at the upper and lower temperatures was achieved. To check that the salt was undergoing a melt/freeze cycle a thermocouple was used to measure the temperature of the salt, the output of which are presented in Fig. 2.

Upon removal from the furnace, samples were cooled slowly in another furnace to reduce thermal shock, which can cause corrosion layers to split and spall. Once cool, solid salt/metal samples were removed from the crucibles and the exposed section of the metal was cut from the top of the salt and mounted separately in conductive epoxy. This exposed sample was wet sanded with 320 grit SiC foil then progressively polished with 9 µm, 3 µm, 1 µm and 0.04 µm polishing suspensions. The submerged sample and salt block was cut in cross-section using a precision saw run at low speed and force to minimise damage. The cross section was progressively sanded smooth using SiC foil up to 2000 grit. Polishing was undertaken using 6 µm, 3 µm and 0.25 µm diamond paste and kerosene as a polishing fluid to prevent the salt from dissolving. This method allows critical salt/corrosion interface information to be retained in the samples and has been described in detail elsewhere (Lippiatt, 2021). Samples were stored at 50 °C to prevent hydration due to humidity and prior to SEM-EDS analysis, they were coated with a 10 nm thick carbon layer to prevent charging.

Samples from cylindrical wire were used, as any errors due to geometry or misalignment during mounting and cross-sectioning would be easily identifiable. If significant corrosion occurs, a thickness loss corrosion rate can be determined by comparing the minimum diameter of corroded and uncorroded samples. Using thickness loss measurements for corrosion rate determination is preferred over mass loss based methods as the small weight changes measured can lead to excessive errors, particularly if tenacious corrosion products remain, or the cleaning method removes base metal. It also allows corrosion rate and analysis of the scale morphology de-alloying, and metal microstructure to be undertaken on the same sample.

A Leica M125 Zoom Stereo Microscope was used to obtain images of

Table 1

Diameter and elemental composition of alloy 625 wire (from supplier Certified Material Test Report).

Alloy	Dia (mm)	Ni	Cr	Fe	Mo	Nb + Ta	Ti	Mn	Cu	Si	Co	Al	C	S
625	2.4	64.3	22.3	0.2	9.1	3.55	0.21	0.2	<0.01	0.07	0.03	0.1	0.01	0.001

Table 2

Test Matrix for isothermal and thermally cycled testing.

Alloy	96 h	192 h	384 h	768 h
625	Isothermal Cycled	Isothermal Cycled	Isothermal Cycled	Isothermal Cycled

the full sample cross section, and image processing software was used to measure sample diameter. SEM images were obtained using a JEOL 7001F Scanning Electron Microscope with an Oxford XMax 80 X-ray EDS detector for elemental mapping. Large samples of approximately 10 g of salt were removed away from the metal sample to minimise inclusion of insoluble corrosion product. The salt samples were ground in a mortar and pestle until a homogeneous powder was obtained. Approximately 0.25 g samples of this powder were dissolved into 50 ml of a solution of 2 % nitric acid and trace concentration hydrofluoric acid to ensure all elements were fully dissolved. Aliquots of these digestions were analysed using an Agilent 8800 Inductively Coupled Plasma Mass Spectrometer (ICP-MS) to determine elemental concentrations in the salt down to parts per million (ppm in mg/kg).

3. Results and Discussion

3.1. Corrosion Analysis

The diameter measurements for both outside and inside of the corrosion layers are relatively consistent across all samples, conditions and test times. Changes in inner diameter (without corrosion scale) indicate that around 10–15 µm of metal loss is experienced across all samples after 200 h of exposure. This yields a corrosion rate of approximately 120–170 µm/year for both the isothermal and the cycled samples, based on the longest test undertaken here (total test time used for the cycled samples). As the metal loss is not significantly increasing with test time, longer term tests will likely reduce the calculated corrosion rate. Testing with more samples, over significantly longer test periods under industrially relevant conditions is required to determine the long term corrosion rate for this metal/salt combination.

When the outside diameter is subtracted from the inner diameter

then halved to find a scale thickness, it is comparable to the scale thickness measured from the SEM images. Therefore, it can be concluded that there is minimal metal dissolution into the salt under any of the test conditions and oxidation is the main surface corrosion mechanism for this metal/salt combination.

Backscatter SEM and EDS maps of the corrosion layers for the 96 h and 768 h tests are included in Figs. 5–8, and measurements of oxide thickness from all of the samples are summarised in Table 3. The samples submerged in the salt show a dense, adherent layer of oxide of 5–10 µm thickness is produced on the surface upon initial exposure to the salt. After longer exposure times, this layer grows to be approximately 10–20 µm thick. The section of the samples which were exposed to air produce a slightly thicker oxide layer, 15–30 µm thick. Unlike in other alloys exposed to this salt (Bell, 2019, 2022), the oxide growth process for this alloy does not seem to be significantly affected by the thermal cycling process. The corrosion layers in these samples are composed of two sub-layers, an inner layer consisting primarily of nickel–chromium oxide, and an outer layer which is mainly nickel oxide. Other studies have found iron present in similar nickel oxide outer layers, but this was not found in this study as the iron concentration in the base alloy was very low (0.2 wt% compared to 3.4 % and 4.5 % in (Soleimani Dorcheh et al., 2016) and (McConohy and Kruizinga, 2014) respectively).

Some chromium depletion is evident at the outer surface of the samples exposed for longer periods of time, in particular the isothermally exposed which have been under high temperature and high oxygen conditions for the longest. Very little to no chlorine or sodium is found in the oxide layers, implying that the oxide layers are dense and do not allow the salt, or chloride ions to penetrate. Any presence shown in the EDS maps presented in Figs. 3–6 is either due to contamination from the polishing process, or chlorine's presence in the preserved salt.

The effectiveness of nickel plating has been noted to be protective to chromium dissolving salts previously (Olson, 2011; Solimani, 2021). Both studies found the nickel layer acted as a diffusion barrier to chromium, preventing it from being removed from the alloy into the salt. This diffusion barrier effect was found to increase when a chromium oxide inner layer was produced prior to plating, as it forms a barrier to chromium diffusion through the nickel metal coating (Olson, 2011). Although the surface layer involved here is nickel oxide, a similar process may be occurring whereby the chromium diffusion is limited

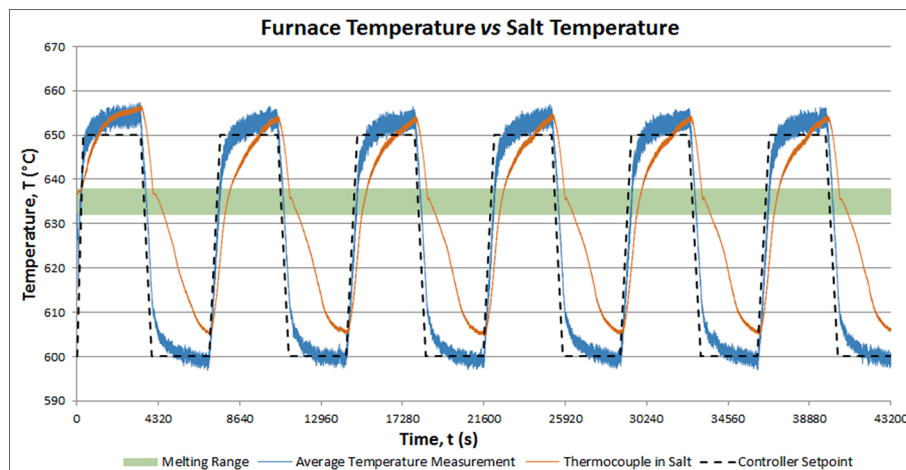
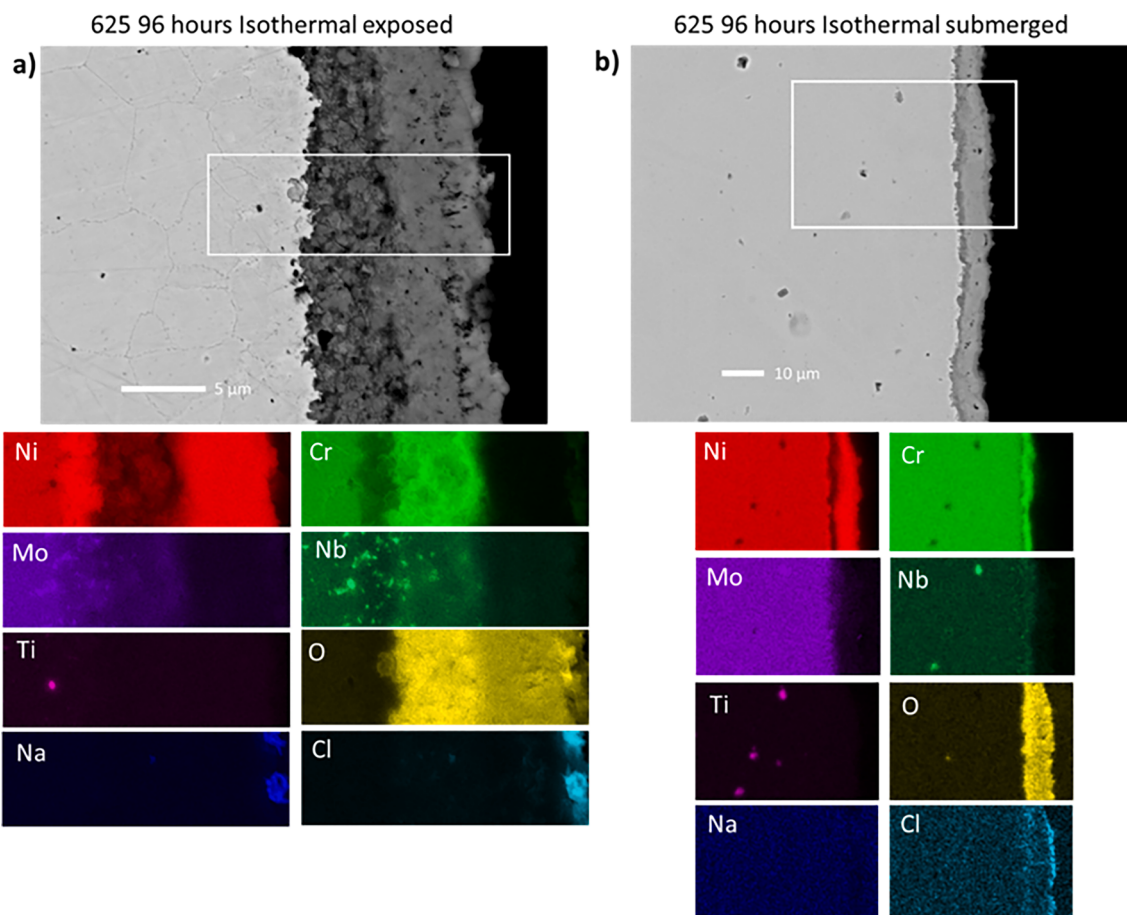


Fig. 2. Temperature data for a thermocouple submerged in salt. Furnace control was based on the average temperature between thermocouples placed at the top and bottom of the furnace.

Table 3Corrosion layer and Depletion analysis of tested samples from SEM analysis (all measurements in μm).

Hours	Scale thickness (SEM)	Cr Depletion	Ni-Cr-O	Ni-O	Scale thickness (SEM)	Cr Depletion	Ni-Cr-O	Ni-O
Isothermal								
Submerged								
96	5.5–10	–	1–3.5	4–7	9–11	2.5	4–5	4.5–5.5
192	13–23	–	3.5–5.5	9–19	17–20	0.5–2.5	4–6	12–14
384	12–18	0–5	3–9	8–14	8–12.5	1–4	4–6.5	4–6
768	11–16.5	2–6	2–7	7.5–11	23–30	1.5–4.5	5.5–9	17–21
Cycled								
Submerged								
Hours	Scale thickness (SEM)	Cr Depletion	Ni-Cr-O	Ni-O	Scale thickness (SEM)	Cr Depletion	Ni-Cr-O	Ni-O
96	6–15	–	5–7.5	2–7	2–4	–	1–3	1–1.5
192	8.5–14	–	3–8.5	4.5–8.5	8.5–14.5	–	3.5–7	5.5–11
384	10–21	–	1.5–8	3.5–18.5	12.5–19	0–3.5	2–3	11–17
768	9.5–16	–	1.5–3.5	8–13.5	15–24	0–2.5	1.5–2.5	14–21

**Fig. 3.** 96 h Isothermally tested Alloy 625 sample a) exposed to air b) submerged in salt. 5–10 μm thick corrosion scale, mostly Ni-O with a Cr-O inner layer.

through the nickel oxide, which is dense and non-porous.

3.2. Salt impurities

Despite the stable and adherent corrosion product, it is obvious from the colour of the salt after the test that some alloying elements are being dissolved from the metal into the salt, as can be seen in Fig. 7. Salts are well known to remove elements such as chromium from stainless steel and nickel superalloys, but usually result in a green hue to the normally white salt due to the Cr^{3+} oxidation state of Cr_2O_3 (Bell, 2019). It is also unlikely to be Cr^{2+} or Cr^{6+} oxidation state responsible for the yellow colour as Cr^{2+} not soluble in this salt and Cr^{6+} was not detected in a

oxidation state study of chromium containing oxide layers produced in this salt (Bell, 2022).

Therefore, the salt was sampled and analysed using ICP-MS, to determine what from the alloy elements were present in the salt. The data from this analysis are presented in Table 4. From this table the alloying elements which are present in the salt are chromium, molybdenum and niobium. The concentrations of all of these elements are relatively low compared to previous studies and the same conditions (Bell, 2019, 2022). There is some scatter to the concentrations measured, which are due to the inhomogeneity in the salt as shown in Fig. 7 b). This is the most evident in the 192 h isothermal sample, which has elevated levels of all three elements relative to the other isothermal

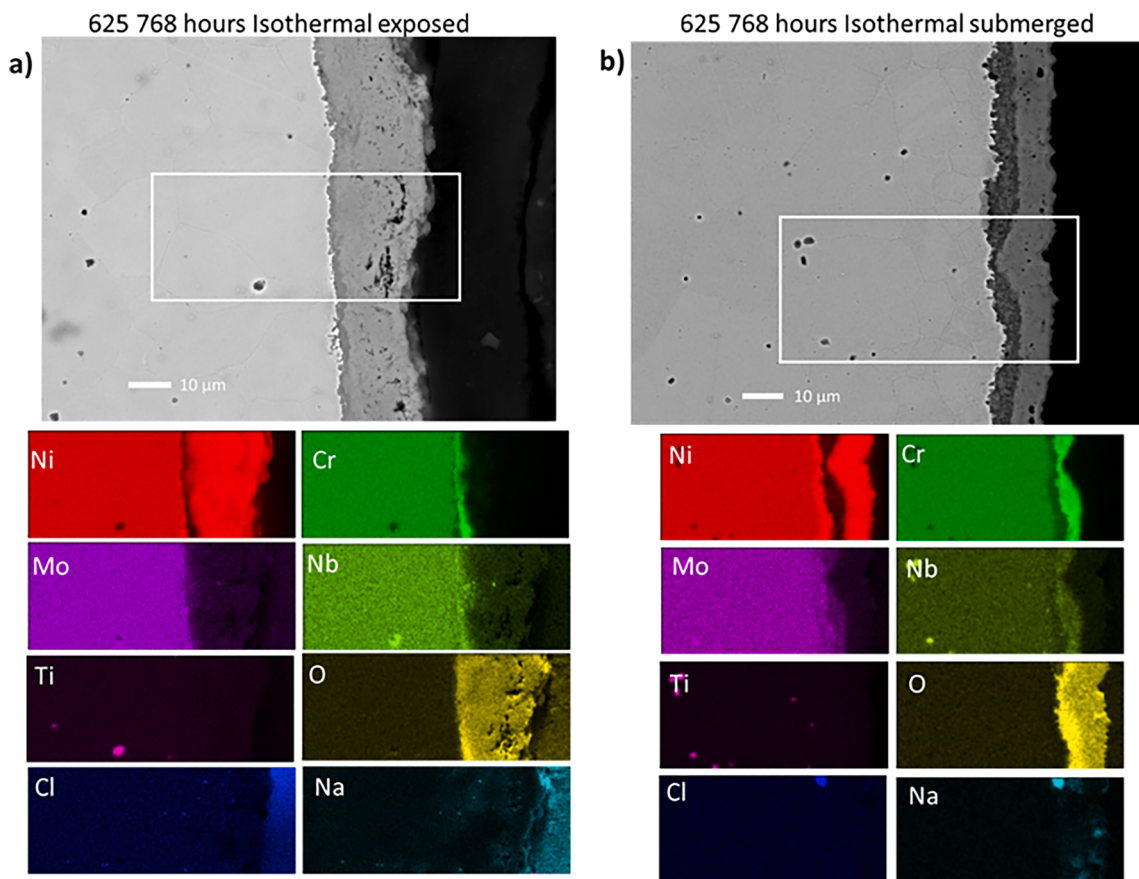


Fig. 4. 768 h Isothermally test Alloy 625 sample a) exposed to air b) submerged in salt. Thicker 10–30 μm thick scale layer, Ni-O layer is primary layer with thin inner layer of Cr-O.

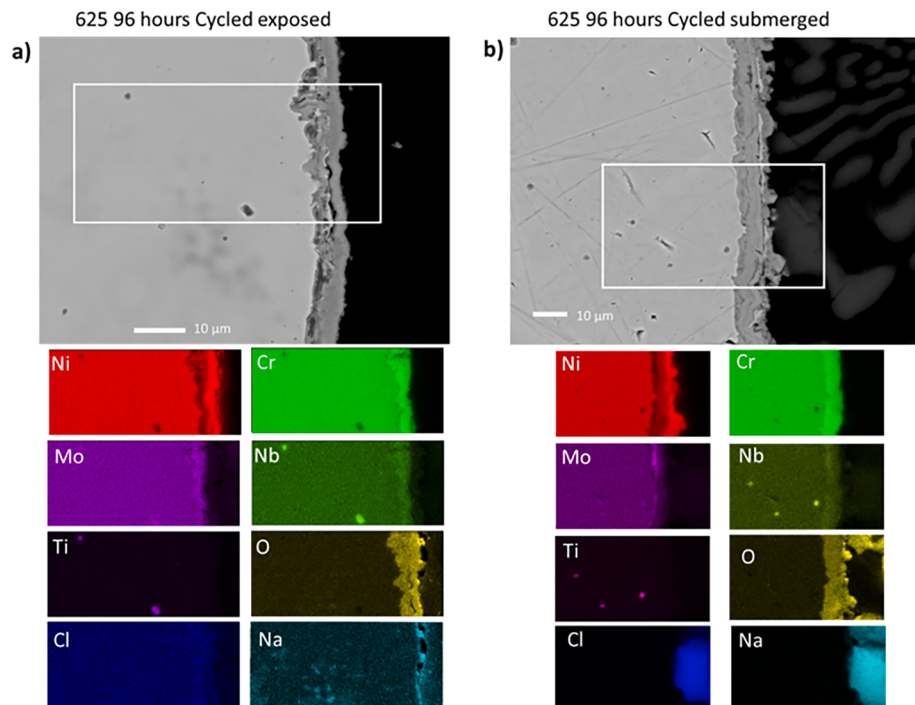


Fig. 5. 96 h Thermally Cycled Alloy 625 sample a) exposed to air, B) submerged in salt. Similar structure to the 96 h Isothermal sample in Fig. 3, slightly thinner oxide layer on exposed sample.

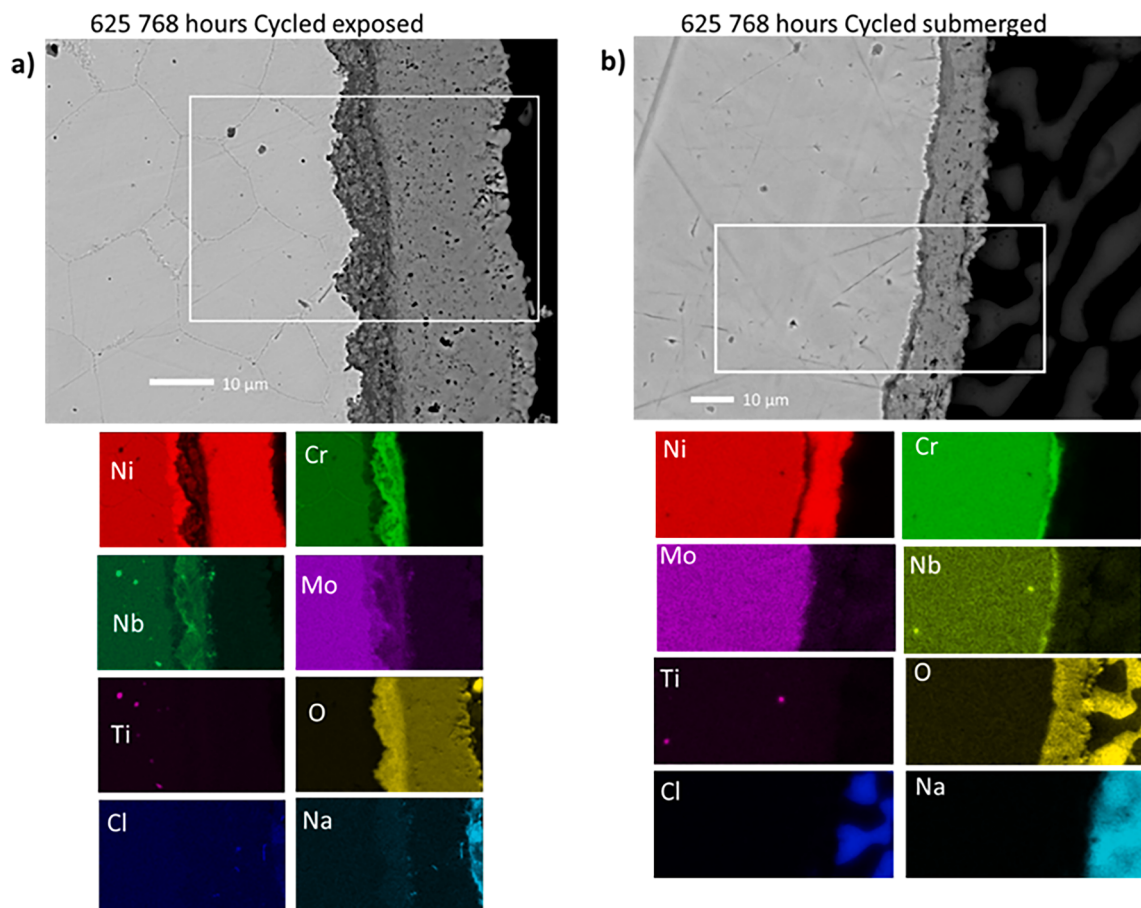


Fig. 6. 768 h Thermally Cycled Alloy 625 sample a) exposed to air, B) submerged in salt. Similar to 768 h isothermal samples in Fig. 4, slightly thinner scale layer on exposed sample.

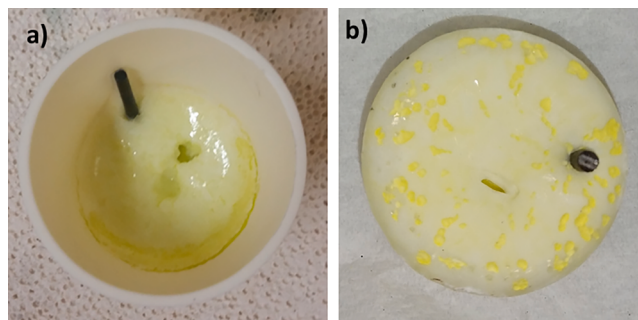


Fig. 7. Salt and metal sample after a) 768 h isothermal test, b) 384 h cycled test.

samples. Interestingly, the concentrations of the isothermal samples for short test times are higher than the cycled samples, but the long term cycled samples are similar to the isothermal samples.

Inconel 625 is a chromium oxide forming alloy in air, but in this salt certain chromium oxide species are soluble and dissolved into the salt, which will happen rapidly from the oxide layers close to the salt. SEM analysis shows chromium rich inner layers in both cycled and isothermally tested samples, and little sub-surface chromium depletion beyond what would occur in an air environment due to Cr_2O_3 formation. As the outer nickel oxide scale layer appears to be stable, further chromium dissolution is probably limited by solid state diffusion through the nickel oxide outer scale layer. This dense oxide layer and was not present on the alloys in the previous studies.

The cycled samples spend approximately 50 % of the time of the isothermal samples exposed to liquid salt at 650 °C, and the rest at

Table 4

Concentrations of alloying elements present in salt (given in ppm).

alloy 625	Ni	Cr	Fe	Mo	Nb	Ti	Mn	Cu	Si	Co	Al	S
Alloy wt % Isothermal	64.3	22.3	0.2	9.1	3.55	0.21	0.2	<0.01	0.07	0.03	0.1	0.001
	96 hrs	1.00	58.34	0.96	38.87	7.99	0.34	0.34	0.14	nd	1.41	5.06
	192 hrs	2.01	145.38	1.22	74.73	15.74	0.78	0.41	0.07	4.70	2.04	5.06
	384 hrs	0.83	59.22	1.00	56.86	11.74	0.41	0.42	0.09	2.19	0.94	5.50
Cycled	768 hrs	1.03	118.08	1.01	78.03	13.33	0.61	0.37	0.12	1.89	5.83	4.33
	96 hrs	1.12	9.16	0.70	18.22	1.29	0.10	0.14	0.15	1.55	nd	1.14
	192 hrs	0.23	21.61	0.46	30.06	2.96	0.11	0.14	0.04	1.28	0.55	5.25
	384 hrs	0.47	78.11	0.79	46.49	10.91	0.35	0.15	0.04	1.55	0.95	4.91
	768 hrs	0.34	160.93	1.06	80.20	15.10	0.60	0.20	0.06	2.17	1.19	5.11

nd = not detected.

600 °C exposed to solid salt. This should slow the solid state diffusion process of chromium through the surface oxide. However, these samples also have slightly reduced thickness oxide layers (5–6 µm less in the exposed sections and 2–5 µm less in the submerged sections), which reduce the distance that chromium needs to diffuse when thermally cycled. This shorter diffusion distance could be why slightly more chromium is present in the cycled salt at longer test times than the isothermal salt.

Vulnerability plots, where the ppm content of each alloying element is determined relative to the element's wt% in the alloy, have been used previously to investigate which elements are most likely to be dissolved into the salt (Bell, 2019, 2022). The results of this analysis for the major elements in the alloy (Ni, Cr, Mo, Nb, Ti, Fe, and Mn) are presented in Fig. 8 for the isothermal tests and Fig. 9 for the thermally cycled tests. This approach shows that in addition to molybdenum, chromium and niobium being removed from the alloy, the minor alloying elements iron, titanium and manganese were also found in significant amounts relative to the low concentration in the alloy. This is not immediately noticeable from the raw impurity data. The isothermal data shows that the dissolution of these elements is not significantly increased in the longer immersion tests, potentially encountering a saturation limit in the salt. The cycled data shows that (except for manganese) these concentrations steadily increase with immersion time until a similar overall concentration to the isothermal salt is attained. A likely explanation for this behaviour is both the diffusion rate and elemental solubilities in the salt will be lower at 600 °C than 650 °C, meaning longer immersion times are required for saturation to be reached for samples that spend more than half the time below 650 °C. Additionally, the relative order of elemental vulnerability for both isothermal and cycled samples after 768 h is consistently Mo > Cr > Fe > Nb > Ti > Mn. Nickel, despite being the major alloying element has almost no presence in the salt, confirming that the nickel oxide outer layer is insoluble in the salt.

The vulnerability of molybdenum in this salt is an interesting observation, particularly as molybdenum is often used as a crucible material in high temperature corrosion studies involving liquid metals and halide based molten salts (Barkia, 2018; Pint, et al., 2019). Those tests however, are undertaken under inert atmospheres and in liquids with low oxidative potential. The salt tested here includes an oxygen containing anion which can dissociate, producing carbon dioxide and an oxide ion, via the Lux-Flood reaction for molten salt acidity/basicity (Bell et al., 2019; Lux and Proeschel, 1948). This means that this salt has

the oxidative potential to react with molybdenum and produce molybdenum oxide species. This was discussed in a previous paper by the authors, in which a chloride/sulphate eutectic salt reacted with C-276 alloy producing a number of different products (Bell, 2021). Modelling in this paper using FactSage software suggested that molybdenum would produce Na_2MoO_4 which would be dissolved into the salt as a molybdate ion (MoO_4^{2-}). This molybdenum dissolution mechanism will also occur in a carbonate based salt, and is a potential pathway for molybdenum to be removed and dissolved by the salt.

4. Conclusions

Alloy 625 was tested for its corrosion resistance to $\text{NaCl}/\text{Na}_2\text{CO}_3$ salt under both isothermal conditions at 650 °C and thermal cycling between 600 °C and 650 °C. Tests up to 768 hrs (32 days) were undertaken and analysed using SEM, EDS and ICP-MS. SEM backscatter and EDS Maps determined that alloy 625 was resistant to the salt for up to 768 h. Scale growth was the primary corrosion process, with minimal thickness loss and no major dealloying in either the isothermal or thermally cycled tests. A corrosion rate of approximately 120–170 µm/year was identified, however as this was based on the initial scale growth and 768 h of testing, this is expected to be significantly less over longer exposure. Total scale thicknesses of 15–30 µm were produced on the metal surface with stable 10–20 µm thick nickel oxides layers formed in contact with the salt. Inner nickel–chromium oxide layers 5–10 µm thick developed at the metal surface.

ICP-MS analysis showed relatively minor amounts of dealloying into salt, despite a bright yellow colour formed in the normally white salt. All alloying elements were found to be present in the salt except nickel – which makes up the outer layer of the corrosion scale. Molybdenum, chromium and niobium were present in the highest concentrations, although when original alloy wt% was considered, iron, titanium, and manganese also had some vulnerability. Isothermal samples were found to have minimal increase in dissolution with time, showing fairly consistent concentrations of dissolved elements for all test times. Thermally cycled samples showed a steady increase in dissolution with test time, implying that the movement of these elements into the salt was slowed by the time spent at lower temperatures.

Overall, alloy 625 had good corrosion resistance to this salt under both isothermal and thermally cycling conditions. The combination of chromium rich inner oxide layer, and a dense, adhesive nickel oxide

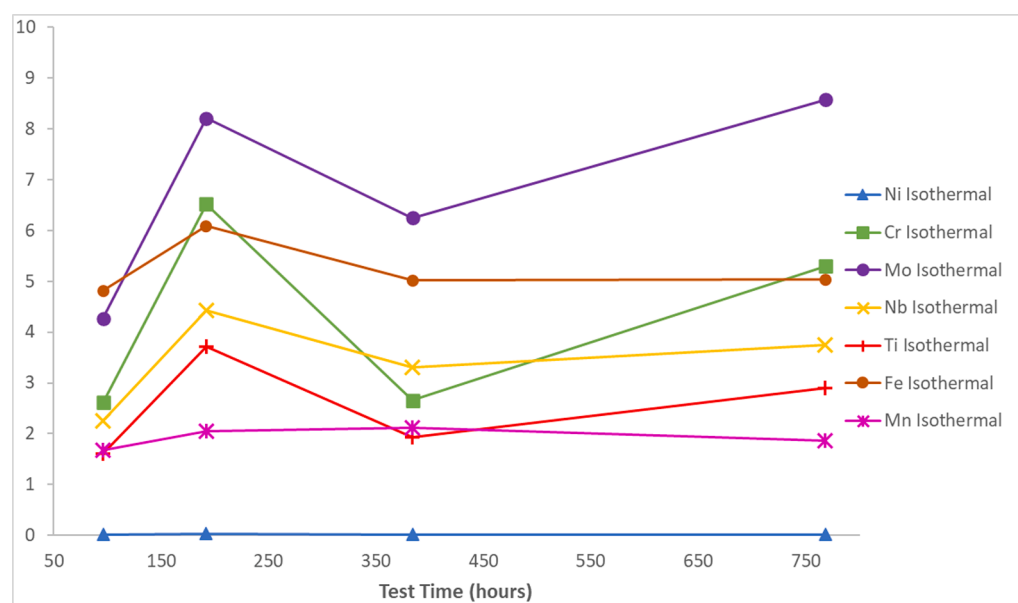


Fig. 8. Ratio of alloy element concentration in salt to wt% in alloy for isothermal tests.

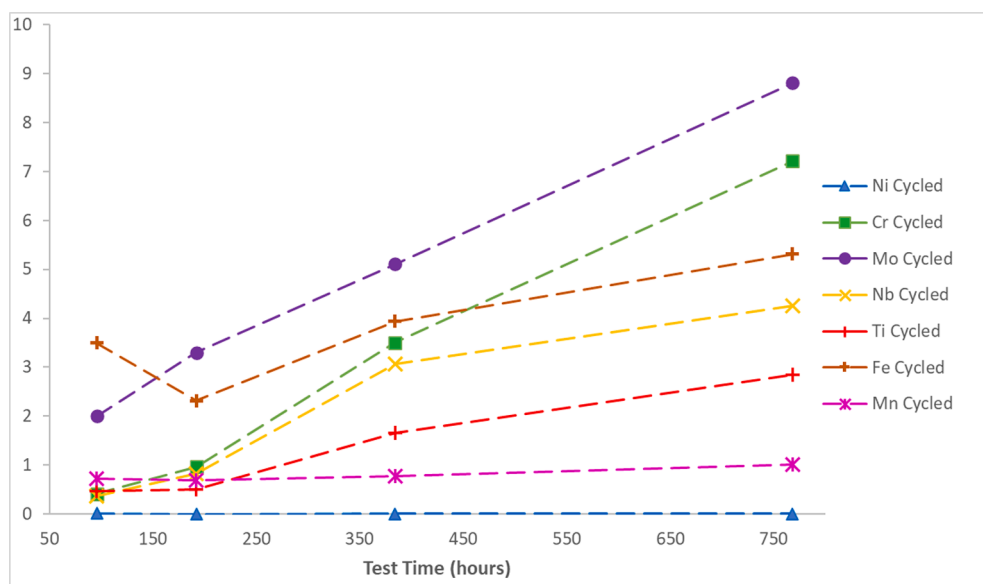


Fig. 9. Ratio of element concentration in salt to wt% in alloy for thermally cycled tests.

outer layer seems to successfully prevent the significant dealloying from the metal seen in other metals in this salt. Further, long term testing could determine if this alloy provides commercial level corrosion resistance to this promising molten salt phase change material.

Declaration of Competing Interest

The authors declare that they have no known competing financial interests or personal relationships that could have appeared to influence the work reported in this paper.

Acknowledgments

This research was performed as part of the Australian Solar Thermal Research Initiative (ASTRI), a project supported by the Australian Government, through the Australian Renewable Energy Agency (ARENA). The data reported in the paper were obtained at the Central Analytical Research Facility (CARF) operated by the Institute for Future Environments at Queensland University of Technology (QUT). Access to CARF was supported by generous funding from the Science and Engineering Faculty, QUT.

References

- Barkia, B., et al., 2018. Wetting by liquid sodium and fracture path analysis of sodium induced embrittlement of 304L stainless steel. *J. Mater. Res.* 33 (2), 121–129.
- Bell, S., et al., 2019. Damage analysis of 601 nickel superalloy in eutectic Na₂CO₃/NaCl molten salt under isothermal and thermal cycling conditions. *Sol. Energy* 191, 637–646.
- Bell, S., et al., 2021. Aggressive corrosion of C-276 nickel superalloy in chloride/sulphate eutectic salt. *Sol. Energy* 227, 557–567.
- Bell, S., et al., 2022. Corrosion mechanism of SS316L exposed to NaCl/Na₂CO₃ molten salt in air and argon environments. *Corros. Sci.* 195, 109966.
- Bell, S., et al., 2022. C-276 nickel alloy corrosion in eutectic Na₂CO₃/NaCl molten salt under isothermal and thermal cycling conditions. *Sol. Energy Mater. Sol. Cells* 240, 111695. <https://doi.org/10.1016/j.solmat.2022.111695>.
- Bell, S., Steinberg, T., Will, G., 2019. Corrosion mechanisms in molten salt thermal energy storage for concentrating solar power. *Renew. Sustain. Energy Rev.* 114, 109328.
- Frangini, S., 2008. Corrosion of metallic stack components in molten carbonates: Critical issues and recent findings. *J. Power Sources* 182 (2), 462–468.
- Gomez-Vidal, J.C., Noel, J., Weber, J., 2016. Corrosion evaluation of alloys and MCraIX coatings in molten carbonates for thermal solar applications. *Sol. Energy Mater. Sol. Cells* 157, 517–525.
- Gomez-Vidal, J.C., Tirawat, R., 2016. Corrosion of alloys in a chloride molten salt (NaCl-LiCl) for solar thermal technologies. *Sol. Energy Mater. Sol. Cells* 157, 234–244.
- Grégoire, B., et al., 2020. Corrosion mechanisms of ferritic-martensitic P91 steel and Inconel 600 nickel-based alloy in molten chlorides. Part II: NaCl-KCl-MgCl₂ ternary system. *Sol. Energy Mater. Sol. Cells* 216, 110675.
- American Iron and Steel Institute, 1979. High-Temperature Characteristics of Stainless Steels. In: A Designers' Handbook Series No. 9004. Nickel Development Institute.
- Jiang, Y., et al., 2016. Eutectic Na₂CO₃-NaCl salt: A new phase change material for high temperature thermal storage. *Sol. Energy Mater. Sol. Cells* 152, 155–160.
- Khorsand, S., et al., 2018. Hot Corrosion Behavior of Inconel 625 Superalloy in Eutectic Molten Nitrate Salts. *Oxid. Met.* 90 (1), 169–186.
- Kondo, M., et al., 2009. High Performance Corrosion Resistance of Nickel-Based Alloys in Molten Salt Flibe. *Fusion Sci. Technol.* 56 (1), 190–194.
- Kruizinga, A.M., 2012. Corrosion Mechanisms in Chloride and Carbonate Salts. Sandia National Laboratories: Albuquerque, New Mexico.
- Lippiatt, K., et al., 2021. An improved technique for molten salt corrosion sample preparation. *Sol. Energy Mater. Sol. Cells* 226, 111057.
- Liu, M., et al., 2016. Review on concentrating solar power plants and new developments in high temperature thermal energy storage technologies. *Renew. Sustain. Energy Rev.* 53, 1411–1432.
- Liu, M., et al., 2017. A eutectic salt high temperature phase change material: Thermal stability and corrosion of SS316 with respect to thermal cycling. *Sol. Energy Mater. Sol. Cells* 170, 1–7.
- Liu, M., et al., 2021. Techno-economic analysis on the design of sensible and latent heat thermal energy storage systems for concentrated solar power plants. *Renew. Energy* 178, 443–455.
- Lux, H., Proeschel, E., 1948. Über das Chrom(II)-oxyd. *Z. Anorg. Allg. Chem.* 257, 73–78.
- McConohy, G., Kruizinga, A., 2014. Molten nitrate salts at 600 and 680 °C: Thermophysical properties changes and corrosion of high-temperature nickel alloys. *Sol. Energy* 103, 242–252.
- Ming, Z., et al., 2015. Effects of Cations on Corrosion of Inconel 625 in Molten Chloride Salts. *High Temp. Mater. Processes* 35 (4), 337–345.
- Olson, L., et al., 2011. Nickel-plating for active metal dissolution resistance in molten fluoride salts. *J. Nucl. Mater.* 411 (1–3), 51–59.
- Ong, T.-C., et al., 2021. An innovative empirical method for the accurate identification of the eutectic point of binary salts for solar thermal energy storage. *Mater. Today Commun.* 26, 101864.
- Pint, B.A., et al., 2019. Re-establishing the paradigm for evaluating halide salt compatibility to study commercial chloride salts at 600°C–800°C. 70(8), p. 1439–1449.
- Raud, R., et al., 2018. Optimized Salt Selection for Solar Thermal Latent Heat Energy Storage. *Adv. Sustain. Syst.* 2 (11), 1800074.
- Raud, R., et al., 2018. Experimental verification of theoretically estimated composition and enthalpy of fusion of eutectic salt mixtures. *Sol. Energy Mater. Sol. Cells* 174, 515–522.
- Sarvghad, M., Will, G., Steinberg, T.A., 2017. Corrosion of Inconel 601 in molten salts for thermal energy storage. *Sol. Energy Mater. Sol. Cells* 172, 220–229.
- Sarvghad, M., Steinberg, T.A., Will, G., 2017. Corrosion of steel alloys in eutectic NaCl+Na₂CO₃ at 700°C and Li₂CO₃ + K₂CO₃ + Na₂CO₃ at 450°C for thermal energy storage. *Sol. Energy Mater. Sol. Cells* 170, 48–59.
- Sarvghad, M., Steinberg, T.A., Will, G., 2018. Corrosion of stainless steel 316 in eutectic molten salts for thermal energy storage. *Sol. Energy* 172, 198–203.
- Soleimani Dorcheh, A., Durham, R.N., Galetz, M.C., 2016. Corrosion behavior of stainless and low-chromium steels and ING25 in molten nitrate salts at 600°C. *Sol. Energy Mater. Sol. Cells* 144, 109–116.
- Solimani, A., et al., 2021. Electroless Ni-P coatings on low-Cr steels: A cost-efficient solution for solar thermal applications. *Sol. Energy Mater. Sol. Cells* 231, 111312.

Special Metals. Product Handbook of High-Performance Nickel Alloys. In: PCC-8064. Precision Castparts Corp: www.specialmetals.com.

Sridharan, K., Allen, T.R., 2013. Corrosion in Molten Salts. In: Lantelme, F., Groult, H. (Eds.), Molten Salts Chemistry. Elsevier, Oxford, pp. 241–267.

Walczak, M., et al., 2018. Materials corrosion for thermal energy storage systems in concentrated solar power plants. Renew. Sustain. Energy Rev. 86, 22–44.